Earth and Planetary Science Letters 365 (2013) 7–16

Contents lists available at SciVerse ScienceDirect

Earth and Planetary Science Letters

journal homepage: www.elsevier.com/locate/epsl

Ferric iron content of ferropericlase as a function of composition, oxygen fugacity, temperature and pressure: Implications for redox conditions during diamond formation in the lower mantle

Kazuhiko Otsuka [a],*, Micaela Longo [b], Catherine A. McCammon [c], Shun-ichiro Karato [a]

[a] *Yale University, Department of Geology and Geophysics, 210 Whitney Avenue, New Haven, CT 06511, USA*
[b] *University of Padua, Department of Geosciences, Via Giotto 1, 35137 Padua, Italy*
[c] *Bayerisches Geoinstitut, Universität Bayreuth, D-95440 Bayreuth, Germany*

ARTICLE INFO

Article history:
Received 18 October 2011
Received in revised form
27 October 2012
Accepted 16 November 2012
Editor: L. Stixrude

Keywords:
iron oxidation state
flank method
ferropericlase
diffusion
lower mantle
diamond

ABSTRACT

We investigated the ferric iron (Fe^{3+}) concentration in (Mg,Fe)O ferropericlase using the flank method applied to Mg–Fe interdiffusion couples of ferropericlase. Diffusion couples with Mg/(Mg+Fe) in the range 0.44 to 1 were annealed at temperatures of 1673–1873 K and pressures of 5–24 GPa over a wide range of oxygen fugacities. Oxygen fugacity was controlled by Fe, Ni, Mo, and Re metal capsules and their corresponding oxide phases. Based on our results and available experimental data, we derived an equation for the Fe^{3+} solubility in ferropericlase applicable to depths at the top of the lower mantle: $[Fe^{3+}]=C\,(X_{Fe}^{4} f_{O2})^{m} \exp\{-((1-X_{Fe})E^{*}_{Mg}+X_{Fe}E^{*}_{Fe}+PV^{*})/RT\}$, where $C=2.6(1)\times 10^{-3}$, $m=0.114(3)$, $E^{*}_{Mg}=-35(3)$ [kJ/mol], $E^{*}_{Fe}=-98(2)$ [kJ/mol], and $V^{*}=2.09(3)$ [cm^{3}/mol]. The value of the oxygen fugacity exponent m implies that Fe^{3+} mostly occupies tetrahedral sites under these conditions, which is consistent with the results of previously reported Mössbauer spectroscopy studies. Based on this relationship, we calculated the redox conditions of ferropericlase inclusions in diamonds believed to have come from the lower mantle. The estimated oxygen fugacities are close to the upper stability limit of diamond in mantle peridotite at the top of the lower mantle at adiabatic or slightly superadiabatic temperatures, which suggests that ferropericlase inclusions recorded and preserved the conditions at which diamond was precipitated from carbonates or carbonatite melts near the top of the lower mantle.

1. Introduction

The oxidation state of iron in (Mg,Fe)O ferropericlase, the second most abundant phase in the lower mantle, has an important influence in controlling the chemical and physical behavior of the material. The variation in its oxidation state affects various transport properties such as atomic diffusion (Mackwell et al., 2005), electrical conductivity (Dobson. et al., 1997; Hansen and Cutler, 1966; Wood and Nell, 1991) and rheological properties (Gordon, 1973; Tremper et al., 1974) through its influence of point defect populations. Small amounts of Fe^{3+} (or the oxygen fugacity) can affect phase relations and element partitioning between ferropericlase and coexisting phases, including melting relationships (Frost and McCammon, 2008; Gessmann et al., 1999; Rohrbach and Schmidt, 2011).

Laboratory studies on Fe^{3+} solubility in ferropericlase have been conducted at room pressure (Dobson et al., 1998; Hilbrandt and Martin, 1998; Katsura and Kimura, 1965; O'Neill et al., 2003; Speidel 1967; Srečec et al., 1987; Wiser and Wood, 1991) and at high pressures (Bolfan-Casanova et al., 2002; Frost and Langenhorst, 2002; McCammon et al., 2004a; Otsuka et al., 2010; Sinmyo et al., 2008a, 2008b). It is generally assumed that Fe^{3+} is the most dominant positively charged point defect in ferropericlase (e.g., Hazen and Jeanloz, 1984), although ferropericlase dissolves other trivalent cations such as Al^{3+}, Cr^{3+}, and monovalent cations such as Na^{+}, K^{+}, and H^{+} (Bolfan-Casanova et al., 2002; Irifune et al., 2010; Wood, 2000). In the case where sufficient monovalent cations are not available to maintain charge neutrality conditions, the substitution of trivalent cations is charge compensated by the creation of cation vacancies. In ferropericlase these are predominantly created by chemical impurities in the extrinsic regime, which dominate over thermally activated Schottky defects in the intrinsic regime (e.g., Van Orman et al., 2009). Therefore, vacancy concentrations can be obtained by measuring impurity concentrations, rather than by calculating the free energy of vacancy formation (e.g., de Koker and Stixrude, 2010).

The concentration of Fe^{3+} in ferropericlase changes by orders of magnitude with variation of thermochemical parameters such as oxygen fugacity, chemical composition, temperature, and pressure (e.g., Otsuka et al., 2010). The precise knowledge of solubility of Fe^{3+} and other cations is critical to constrain the charge neutrality conditions and the behavior of transport properties. Furthermore, an understanding of Fe^{3+} solubility provides

---

* Corresponding author. Tel.: +1 203 432 5791; fax: +1 203 432 3134.
E-mail address: kazuhiko.otsuka@yale.edu (K. Otsuka).

0012-821X/$ - see front matter © 2013 Published by Elsevier B.V.
http://dx.doi.org/10.1016/j.epsl.2012.11.030

an experimental basis for inferring the oxygen fugacity and other thermochemical states in the lower mantle from ferropericlase inclusions encapsulated in diamond believed to have been derived from the lower mantle (Brenker et al., 2002; Harte, 2010; Hayman et al., 2005; Hutchison et al., 2001; McCammon et al., 1997, 2004b; Stachel et al., 2000).

Several techniques are available to determine the oxidation state of Fe, including the Mössbauer spectroscopy (e.g., McCammon, 2004), electron energy loss spectroscopy (e.g., van Aken and Liebscher, 2002), X-ray absorption near edge structure spectroscopy (e.g., Cottrell et al., 2009), and techniques using an electron probe (e.g., Höfer et al., 1994). As one of the methods involving an electron microprobe, the flank method has several advantages compared with other techniques. The flank method permits simultaneous determination of the oxidation state of Fe and the major element chemistry on the same analytical point, which minimizes systematic biases that might appear between separate measurements. It has relatively high spatial resolution (on the order of 1 μm), large spatial coverage (up to cm-sized samples), and short acquisition time (on the order of a few tens of minutes). These features make it suitable to determine Fe^{3+} contents in heterogeneous samples such as the diffusion couples explored in this study.

The flank method analyzes the variation of Fe$L\alpha$ and Fe$L\beta$ X-ray emission spectra caused by different valence states of Fe using a hybrid approach that incorporates both the $L\beta/L\alpha$ intensity ratios and the peak shift (Höfer et al., 1994). The spectrometer positions of the wavelength dispersive system are set to the positions on the flanks of the Fe$L\alpha$ and Fe$L\beta$ emission lines where Fe^{2+} and Fe^{3+}-bearing samples exhibit the largest difference to each other. Since X-ray emission spectra are sensitive to the crystal structure, it is necessary to construct a calibration curve specific to each mineral species (Höfer and Brey, 2007). So far, the flank method has been successfully applied to sodic amphibole (Enders et al., 2000), garnet (Höfer and Brey, 2007), and ferropericlase (Höfer et al., 2000; Longo et al., 2011).

In this article, we report an investigation of the oxidation state of Fe using the flank method applied to Mg–Fe interdiffusion couples of ferropericlase with a wide range of chemical composition annealed at different pressures, temperatures and oxygen fugacities. Our results enable the derivation of an equation for Fe^{3+} solubility in ferropericlase applicable to depths at the top of the lower mantle, which can be used to infer the conditions at which ferropericlase inclusions in the lower mantle diamonds may have formed.

2. Experiments

2.1. Sample synthesis

The ferropericlase single crystals for high-P,T diffusion experiments were prepared by Mg–Fe interdiffusion between single crystal MgO periclase and mixtures of periclase and Fe_2O_3 hematite powder annealed at 1873 K for 200–300 h at an oxygen fugacity of 1 Pa in a gas-mixing furnace, following previously reported procedures (Otsuka et al., 2010). The observation of synthesized ferropericlase crystals by a field-emission-gun electron probe micro-analyzer (JXA-8530 F) confirmed that the chemical composition varied by less than a few % in molar Mg/(Mg+Fe) ratio over the sample size used for high-P,T experiments. No detectable contamination of elements other than Fe, Mg, and O was observed. Subsequently, the ferropericlase samples were polished and drilled into cylindrical shapes with thicknesses from 0.5 to 0.8 mm and diameters of 1.4, 1.2, or 1.0 mm, depending on the capsule size for high-P,T experiments. The periclase single crystals that were used as one half of the diffusion couple were prepared in a cylindrical shape with thicknesses from 0.2 to 0.5 mm. Although ferropericlase is isotropic with respect to diffusion in cubic symmetry, the diffusion interface was oriented close to the (100) surface.

2.2. Mg–Fe interdiffusion experiments

The high-P,T Mg–Fe interdiffusion experiments were performed using diffusion couples typically composed of two single crystals of periclase and ferropericlase, and, in some experiments, a single crystal of periclase surrounded by mixtures of periclase and hematite at 5–24 GPa and 1673–1873 K for 2.5–27 h (Table 1). The diffusion couples were loaded into an inner Re, Mo, Ni, or Fe metal capsule in order to control redox state of the experimental charges (Rubie et al., 1993). In addition, ReO_2 or MoO_2 oxides were added to the Re or Mo inner capsules, respectively, while no oxides were typically added to Ni or Fe capsules since NiO and FeO are miscible in ferropericlase. The sample charge in the inner capsule was enclosed in the Pt outer capsule, which was sealed by welding to minimize water exchange with the surrounding environment.

The Pt capsules containing the sample charges were set into 18/11, 14/8, or 8/3 octahedral assemblies. Each assembly consists of the following ceramic and metal parts: a semi-sintered Cr_2O_3-doped MgO octahedron or a MgO+spinel injection-molded octahedron (Leinenweber et al., 2006) with an edge length of 18, 14 or 3 mm as a pressure medium, a ZrO_2 thermal insulation sleeve, a graphite or $LaCrO_3$ stepped cylindrical furnace, a MgO or BN sleeve which insulates the sample capsule from the furnace, and Mo electrodes. Temperature was monitored using a W_5Re–$W_{26}Re$ thermocouple with the thermocouple junction placed in direct contact with one end of the sample capsule. The ceramic parts were fired at approximately 1000 K overnight before assembling.

The octahedral assemblies were loaded into a 1000-ton Kawai-type multi-anvil apparatus installed at Yale University. The confining pressure was exerted on the cell assembly by eight tungsten carbide cubes with an edge length of 26 mm and corner truncations of 11, 8, or 3 mm. Sample pressure was calibrated against hydraulic oil pressure using the following phase transformations: quartz–coesite (Bose and Ganguly, 1995) and coesite–stishovite (Zhang et al., 1996) at 1473 K for the 18/11 assembly, coesite–stishovite and forsterite–wadsleyite in Mg_2SiO_4 (Katsura et al., 2004) at 1673 K for the 14/8 assembly, and wadsleyite–ringwoodite in Mg_2SiO_4 (Inoue et al., 2006) and ringwoodite–perovskite+periclase in Mg_2SiO_4 (Fei et al., 2004) at 1873 K for the 8/3 assembly (see supplementary information). We found that the MgO+spinel injection-molded octahedron exhibited slightly better pressure-efficiency than the commonly-used Cr_2O_3-doped MgO octahedron, probably due to the higher inherent strength of the material as well as its lower porosity.

3. Analytical procedures

3.1. Electron probe microanalysis

We carried out flank method and quantitative elemental analysis on the synthesized Mg–Fe interdiffusion couples using a Jeol XA-8200 electron microprobe equipped with five wavelength dispersive spectrometers at Bayerisches Geoinstitut (BGI) following the procedures reported previously (Longo et al., 2011). We also analyzed the interdiffusion couples using a field-emission-gun electron probe micro-analyzer (JXA-8530 F) with a wavelength dispersive system and a scanning electron microscope (XL30 ESEM-FEG) at Yale University. The analytical conditions for the flank method and major element chemistry analysis were an acceleration voltage of 15 kV and a beam current of 80 nA with a focused electron beam at BGI, and 10 kV and 10 nA at Yale. For the flank method, we measured the Fe$L\alpha$ and Fe$L\beta$ X-ray intensities at the peak flank positions of 706.4 and 716.3 eV using

Table 1
Experimental conditions

Run no.	*P* [GPa]	*T* [K]	Time [min]	Diffusion pairs		Capsule		Added to sample	fO_2 buffer	
				Phase	X_{Mg}	Outer	Inner		Assemblage	ΔMMO
K1118	5	1873	482	Per-Fp	100–64	Pt	Fe	–	Fe, FeO	0.61
K1028	5	1873	301	Per-(Per+Hem)	100–60	Pt	Mo	–	Mo, MoO_2(m)	–
K1027	5	1873	165	Per-(Per+Hem)	100–60	Pt	Ni	–	Ni, NiO(s), NiO(m)	–
K1025	5	1873	150	Per-Fp	100–81	Pt	Re	ReO_2	Re–ReO_2	0
K1026	5	1873	150	Per-(Per+Hem)	100–60	Pt	Re	–	Re–ReO_2	0
K993	15	1673	1620	Per-Fp	100–74	Pt	Mo	MoO_2, Mo	Mo–Mo_2O_3	0**
K991	15	1873	240	Per-Fp	100–79	Pt	Mo	MoO_2, Mo	Mo–Mo_2O_3	−0.15**
K999	15	1873	240	Per-Fp	100–75	Pt	Ni	NiO	Ni–NiO	−0.35/−0.78*
K997	15	1873	180	Per-Fp	100–79	Pt	Re	ReO_2, Re	Re–ReO_2	0
K1126	24	1873	480	Per-Fp	100–48	Pt	Fe	–	Fe(s)–Fe(m)–FeO	–
K1124	24	1873	260	Per-Fp	100–48	Pt	Mo	MoO_2	Mo–Mo_2O_3(m)	–
K1125	24	1873	240	Per-Fp	100–44	Pt	Ni	–	Ni–NiO	−1.19/−2.00*
K1123	24	1873	180	Per-Fp	100–49	Pt	Re	ReO_2	Re–ReO_2	0

P=pressure, *T*=temperature
Phase: Per=MgO single crystals, Fp=(Mg,Fe)O single crystals, Per+Hem=Fe_2O_3 and MgO polycrystal mixture.
XMg: chemical composition of diffusion pairs (Mg/(Mg+Fe+Ni) × 100 in mol).
Added to Sample: materials added to sample in the inner capsule.
Assemblage: redox assemblage to control fO_2. (s): solid phase; (m): liquid phase. Solid phases otherwise indicated.
ΔMMO: $\log fO_2 - \log fO_2$[MMO].

* Estimated from FFO buffer.

** Assumed MoO_2. See text for details.

two thallium acid phthalate (TAP) dispersion crystals with a detector slit size of 300 μm. The collecting time was 180 sec for the flank method and 20 s for the major element chemistry. At the beginning of the electron probe session, the spectrometer positions were calibrated using almandine and andradite standards at 15 kV and 100 nA to determine the maximum and minimum energies of the difference spectrum (Höfer and Brey, 2007). Since the accuracy of the flank method critically depends on the reproducibility of the spectrometer positions (Höfer et al., 2000), we periodically repeated the measurements of $L\beta/L\alpha$ on the almandine standard during the electron probe sessions (Fig. 1). The observed variation of the $L\beta/L\alpha$ intensity ratios over the entire period ($1\sigma=0.067$) is comparable to the standard deviation of each measurement expected from counting statistics ($1\sigma=0.054$ on average). This indicates that there is no significant shift in the spectrometer positions during this period. Therefore, we are confident that a good estimation of $L\beta/L\alpha$ intensity ratios is obtained by averaging the values of each set of measurements.

3.2. Flank method standards

We prepared synthetic ferropericlase standards to obtain a calibration curve for the flank method (Table S1 in Supplementary Material). The standards cover a wide compositional range of total Fe, ∑Fe, from 2 to 49 wt% and ferric iron ratios, $Fe^{3+}/\sum Fe$, from 1% to 15%. Some of these standards have been documented previously (Longo et al., 2011; Otsuka et al., 2010). We also employed the Fe-rich half of the ferropericlase diffusion couples as part of our standard set when ∑Fe was found to be homogeneous. Additionally, well compacted polycrystalline ferropericlase standards were synthesized from periclase–hematite mixtures annealed at 15 GPa and 1873 K for 3 h with Mo and Re capsules (K1111), and at 5 GPa and 1873 K for 2.5 h with a Fe capsule (K1134).

The $Fe^{3+}/\sum Fe$ ratios of the ferropericlase standards were measured using point source Mössbauer spectroscopy. As in previous studies, ^{57}Fe Mössbauer spectra were recorded at room temperature and pressure with transmission geometry on a constant acceleration spectrometer with a ^{57}Co radioactive γ-ray source in a Rh matrix.

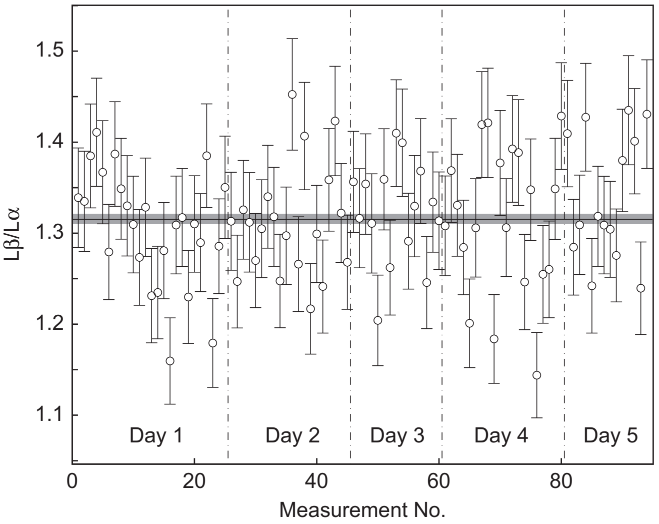

Fig. 1. Reproducibility tests on almandine standards. The data are grouped based on the measurement date. The open circles indicate each measurement and error bars correspond to 1σ uncertainty (from 0.047 to 0.061) estimated from the Fe$L\alpha$ and Fe$L\beta$ intensities assuming a Poisson distribution. This uncertainty is comparable to the observed variation of the $L\beta/L\alpha$ intensity ratios over the entire period (0.067; 1σ). We thus conclude that the spectrometer shift is not significant during this period. The gray bar indicates the 1σ deviation of the mean $L\beta/L\alpha$ value from all of the independent measurements. We obtained a mean value of 1.3152 ± 0.0056 (1σ).

The velocity scale of the spectrometer was calibrated relative to α-Fe foil with 25 μm thickness. Ta foil (25 μm thick) with a 400–500 μm hole was placed over the sample to be measured. The obtained spectra were fitted using the commercially available computer software NORMOS. We fitted the spectra with one Fe^{2+} doublet and one Fe^{3+} doublet assuming Voigt lineshape. The $Fe^{3+}/\sum Fe$ ratios were calculated from the relative area of the Fe^{3+} absorption with a correction for the different recoil-free fractions at room temperature: 0.760 for Fe^{2+} and 0.866 for Fe^{3+} calculated from Mössbauer Debye temperatures of 390 and 550 K, respectively, based on the Debye model (McCammon, 2004). The correction for the recoil-free fraction difference was made for the results of Otsuka et al. (2010), which reduces the Fe^{3+} estimate by approximately 11% of the original value.

3.3. *Flank method calibration*

We followed the procedures of Höfer and Brey (2007) to establish the flank-method calibration. We first collected the Fe$L\alpha$ and Fe$L\beta$ emission lines of ferropericlase standards whose $\mathrm{Fe}^{3+}/\sum\mathrm{Fe}$ ratios were already determined by Mössbauer spectroscopy. We typically measured the Fe$L\alpha$ and Fe$L\beta$ intensities at a minimum of 10 different locations in order to achieve better statistics. The uncertainties of $L\beta/L\alpha$ intensity ratios were estimated by accumulating Fe$L\alpha$ and Fe$L\beta$ intensities of all measurements. The minimum uncertainly in $L\beta/L\alpha$ values were found to be 0.01. Flank method measurements were performed in two different sessions. $L\beta/L\alpha$ intensity ratios measured in different sessions should normally be the same for each sample, but in this case there were systematic differences likely due to a change in the software which slightly altered the energies at which Fe$L\alpha$ and Fe$L\beta$ were measured. Thus we treated each data set from the two sessions separately by constructing two different calibration curves. Results obtained on the same standards are consistent within the two separate sessions and are summarized in Table S1 in Supplementary Material. In Fig. 2 the $L\beta/L\alpha$ intensity ratios of the standards are plotted against total Fe, $\sum\mathrm{Fe}$, obtained from electron probe data. The $L\beta/L\alpha$ intensity ratios increase with $\sum\mathrm{Fe}$ and decrease with Fe^{3+} concentration.

The relatively larger uncertainty in $L\beta/L\alpha$ values at low $\sum\mathrm{Fe}$ is due to the lower count rate at such concentrations.

To quantify Fe^{3+} concentration, we constructed flank method calibration curves by applying a regression model which takes into account the selective self-absorption of the generated FeL X-ray emission by the Fe atoms in the sample (e.g., Höfer et al., 1994). As Longo et al. (2011) reported previously, the relation between $L\beta/L\alpha$ intensity ratios and $\sum\mathrm{Fe}$ becomes non-linear as $\sum\mathrm{Fe}$ increases (Fig. 2), indicating the non-linear self-absorption of Fe atoms. We thus employed the following calibration formula by taking Fe^{2+} as the dependent variable:

$$\mathrm{Fe}^{2+} = A + B \times \sum\mathrm{Fe} + C \times \left(\sum\mathrm{Fe}\right)^2 + D \times \left(\frac{L\beta}{L\alpha}\right) + E \times \sum\mathrm{Fe} \times \left(\frac{L\beta}{L\alpha}\right), \tag{1}$$

where Fe^{2+} and $\sum\mathrm{Fe}$ are ferrous iron and total iron (in wt%), $L\alpha$ and $L\beta$ are the X-ray emission intensities at the Fe$L\alpha$ and Fe$L\beta$ peak flanks, and A, B, C, D, and E are the coefficients. The form of Eq. (1) is similar to the one proposed by Longo et al. (2011), but with more terms which were found necessary to describe adequately the greater range of variation of $L\beta/L\alpha$ values. Results of least squares regressions of measured values are listed in Table S2 in Supplementary material. To illustrate the effect of Fe^{3+} contents on the variation of $L\beta/L\alpha$ ratios, Eq. (1) was solved for 0%, 5%, 15%, and 20% of $\mathrm{Fe}^{3+}/\sum\mathrm{Fe}$ ratios and plotted in Fig. 2. The spacing between the Fe^{3+} isopleths increases with $\sum\mathrm{Fe}$, indicating that $\sum\mathrm{Fe}$ increases the degree to which $L\beta/L\alpha$ intensity ratios depend on Fe^{3+} contents.

Fig. 3 shows the Fe^{3+} concentration of ferropericlase standards estimated by the flank method compared with Mössbauer results. Fe^{3+} determination using those two methods agrees reasonably well, giving a correlation coefficient of 0.96 and 0.97 for the two calibration datasets. The 1σ uncertainties plotted in the figure reflect the inherent nature of the methods. The accuracy in determining Fe^{3+} concentration by Mössbauer spectroscopy decreases with $\sum\mathrm{Fe}$ because the Mössbauer method determines $\mathrm{Fe}^{3+}/\sum\mathrm{Fe}$ ratios with absolute uncertainties typically close to 1–2%. On the other hand, the precision of the flank method increases with $\sum\mathrm{Fe}$ because of two reasons: the variation of the $L\beta/L\alpha$ intensity ratio with a constant Fe^{3+} range increases with increasing $\sum\mathrm{Fe}$ (Fig. 2), and the Fe$L\alpha$ and Fe$L\beta$ emission intensities for a given collecting time also increases with $\sum\mathrm{Fe}$. Thus, the Fe^{3+} concentration determined by the flank method near pure MgO is less reliable than those in the higher Fe part of the composition range (Figs. 2 and 3).

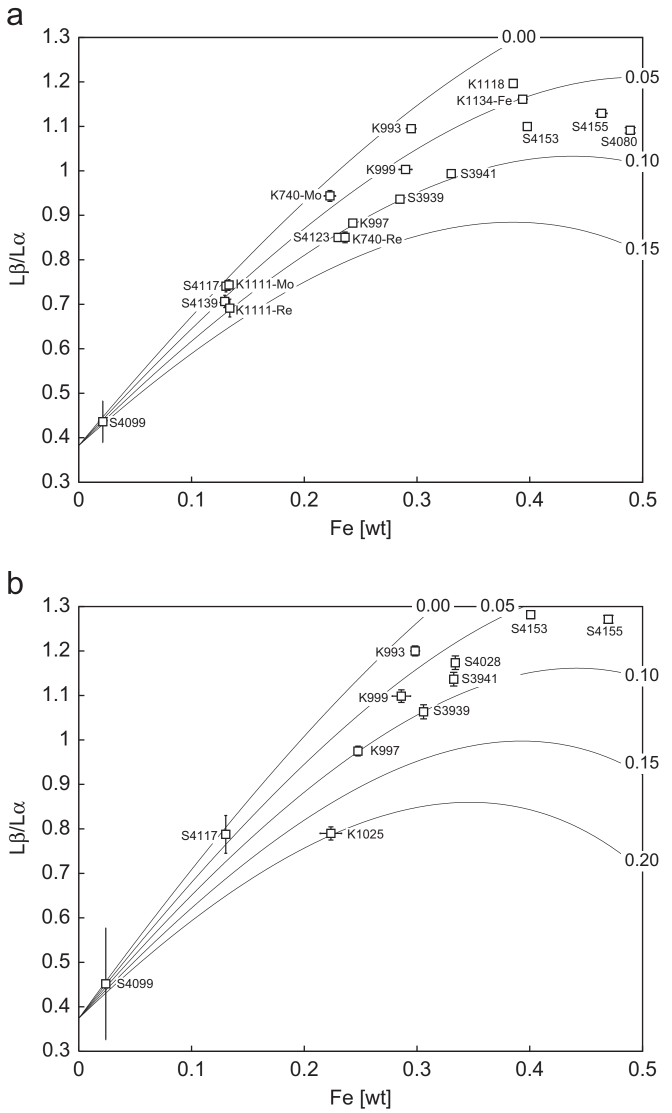

Fig. 2. $L\beta/L\alpha$ intensity ratios obtained for synthetic ferropericlase standards plotted against the total Fe weights, $\sum\mathrm{Fe}$ for two different sessions (a and b). The vertical and horizontal error bars correspond to the 1σ deviation of the mean $L\beta/L\alpha$ value and $\sum\mathrm{Fe}$. Isopleths lines with 0%, 10%, 20%, and 30% of $\mathrm{Fe}^{3+}/\sum\mathrm{Fe}$ ratios are calculated from Eq. (1).

4. Results

4.1. *Experimental run products*

We examined the run products recovered from Mg–Fe interdiffusion experiments using backscattered electron imaging (BSI). Fig. 4 illustrates the representative experimental charges. Most of the periclase–ferropericlase diffusion couples contain no secondary phases at the scale of electron probe observations (Fig. 4A, B). However, irregularly and round-shaped quenched melt droplets were observed in ferropericlase annealed at 24 GPa and 1873 K

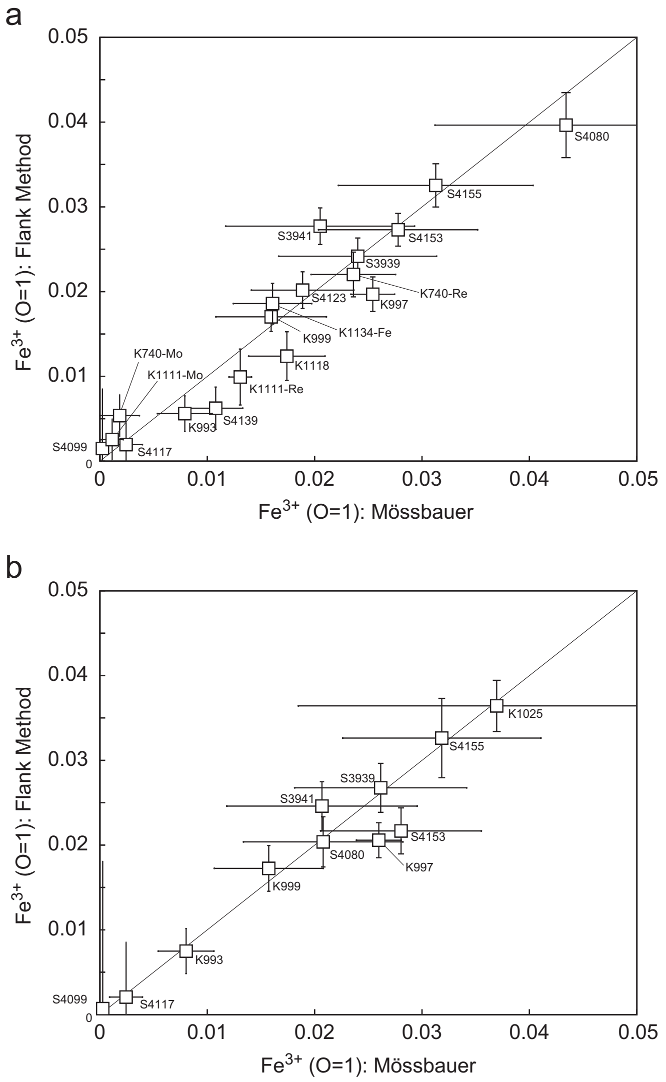

Fig. 3. Fe^{3+} cation abundance in synthetic ferropericlase standards determined by the flank method for two different sessions (a and b) plotted against Fe^{3+} values obtained using the Mössbauer spectroscopy.

with a Fe capsule (K1126; Fig. 4F) and Mo capsule (K1124), whose chemical composition is explained later in this section. In addition, needle-shaped magnesioferrite was uniformly distributed over the Fe-rich side of the ferropericlase diffusion couple annealed at 24 GPa and 1873 K with a Re capsule (K1123; Fig. 4D and E). Mössbauer analysis confirmed the presence of magnesioferrite in another ferropericlase (K1026, annealed at 5 GPa and 1873 K with a Re capsule). Magnesioferrite probably back transformed from its high-pressure polymorph in the $CaMn_2O_4$-type structure on quenching to room pressure and temperature, as previously observed in diamond anvil cell experiments (Andrault and Bolfan-Casanova, 2001).

In order to estimate oxygen fugacity, special attention was given to examination of the redox equilibrium between the metal capsule and its respective oxide. Table S3 in supplementary material reports the chemical composition of the metal capsule and corresponding oxides near the interface between the metal and oxide buffers measured by electron microprobe. For experiments with Re capsules, ReO_2 grains were added to the sample charge in the Re metal capsule, and almost-pure ReO_2 and Re were observed after the diffusion experiments (Fig. 4C). On the other hand, for experiments with Mo capsules, MoO_2 added to the sample charge was reduced to Mo_2O_3-rich oxides for experiments with low Fe contents in diffusion couples (K991, K993), or transformed to quenched Mo oxide-rich melts with dendritic textures with high Fe contents (K1028, K1124). Molten Mo oxide phases wet the grain boundaries of ferropericlase and occasionally were embedded in ferropericlase as inclusions. Mo metal capsules surrounding diffusion couples formed an alloy by dissolving measureable amounts of Pt and Fe. For experiments with a Ni capsule, Ni metal dissolved significant amounts of Fe and Pt, and ferropericlase diffusion couples near the interface of the Ni capsule contained NiO components. NiO-rich melt dissolving a minor amount of Pt was observed along grain boundaries of ferropericlase annealed at 5 GPa and 1873 K (K1027). For experiments with Fe capsules, Fe metal contained some Pt components. Fe–Pt melt was observed within the ferropericlase single crystal annealed at 24 GPa and 1873 K (K1126, Fig. 4F).

Fig. 5 shows representative Mg–Fe interdiffusion profiles obtained at 15 GPa, 1673 K for 27 h in a Mo capsule (K993). The diffusion profile is clearly asymmetric with a long tail on the Fe-rich side, indicating a compositional dependence on diffusivity (e.g., Mackwell et al., 2005). The analysis of diffusion coefficients is part of a separate study and will be published elsewhere.

4.2. *Fe^{3+} contents*

We determined Fe^{3+} contents of the Mg–Fe interdiffusion couples using the flank method, where Fe$L\alpha$ and Fe$L\beta$ intensities were typically measured in steps of 1–3 μm over the diffusion profile. In order to achieve better statistics, Fe$L\alpha$ and Fe$L\beta$ intensities were averaged within the composition window of Fe/(Mg+Fe+Ni) molar ratios of ± 0.02. Fig. 6 shows the obtained Fe^{3+} contents plotted against Fe/(Mg+Fe+Ni) ratios in this study, as well as data from previous studies (Bolfan-Casanova et al., 2002, 2006; Frost and Langenhorst, 2002; McCammon et al., 2004a, O'Neill et al., 2003; Otsuka et al., 2010). Our flank-method results for the Re capsule are generally consistent with the results of Mössbauer studies by Bolfan-Casanova et al. (2006) at 25 GPa and 1873 K for $\sum$Fe of 7% and Otsuka et al. (2010) at 5 and 15 GPa, 1873 K for $\sum$Fe of 20%. Given the relatively larger uncertainty by EELS measurements by Frost and Langenhorst (2002) and McCammon et al., (2004a), the obtained Fe^{3+} concentrations along diffusion profiles are mostly consistent with previous studies at similar conditions.

5. Discussion

5.1. *Attainment of chemical equilibrium*

We first address the attainment of chemical equilibrium in terms of point defect populations, especially Fe^{3+} concentration. The time scale to equilibrate Mg/(Mg+Fe) by diffusion is a few orders of magnitude longer than that for $Fe^{3+}/\sum Fe$, because the equilibration kinetics with respect to Fe^{3+} concentration is rate-limited by diffusion of vacancies and not by the diffusion of atoms (e.g., Rubie et al., 1993). Consequently, there exists an intermediate experimental duration where diffusion flow for $Fe^{3+}/\sum Fe$ vanishes while the concentration gradient of Mg/(Mg+Fe) still exists. The length scale of Fe^{3+} diffusion during our experiments is more than the half width of the sample size. This is supported by the fact that flank-method measurements show small variation in $L\beta/L\alpha$ ratios for the Fe-rich end of ferropericlase diffusion couples (K1025, K997, K999, K993, K1118) and also by the fact that magnesioferrite in K1123 is uniformly distributed throughout ferropericlase. Assuming that the chemical potential gradient of Mg and Fe does not cause diffusion flow of vacancies (see Supplementary Material, S3), the concentration of Fe^{3+}

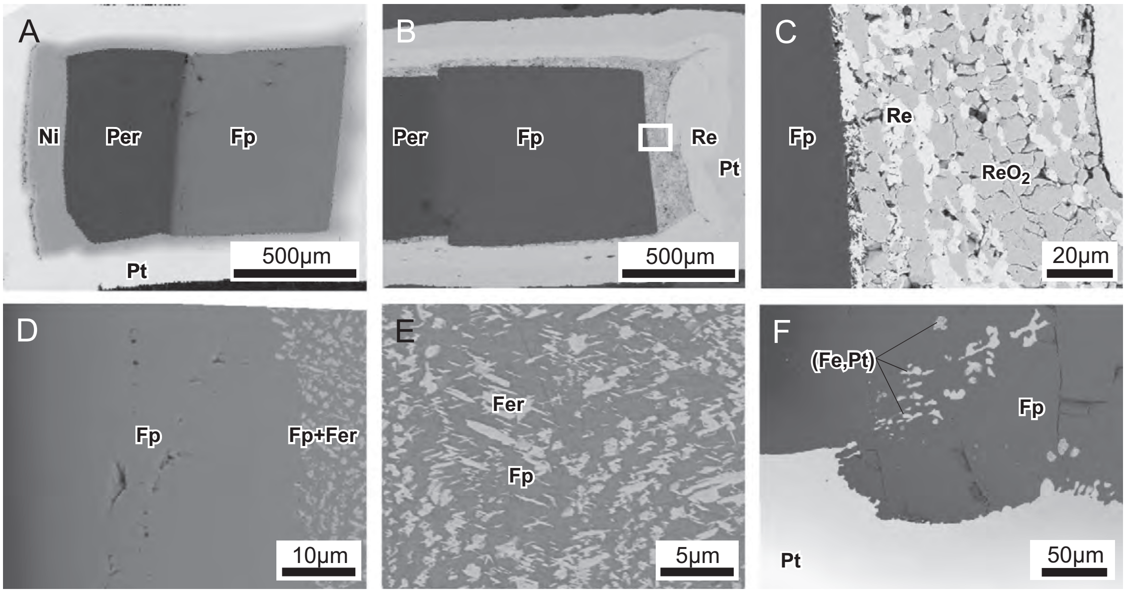

Fig. 4. Backscattered electron images of run products: periclase–ferropericlase diffusion couples annealed at 24 GPa, 1873 K with a Ni capsule (K1125; A), at 15 GPa, 1873 K with a Re capsule (K997; B, and C), 24 GPa, 1873 K with a Re capsule (K1123; D, and E) and 24 GPa, 1873 K with a Fe capsule (K1126; F). (C) is an expansion of the rectangular areas in (B). Per=periclase, Fp=ferropericlase, Fer=magnesioferrite.

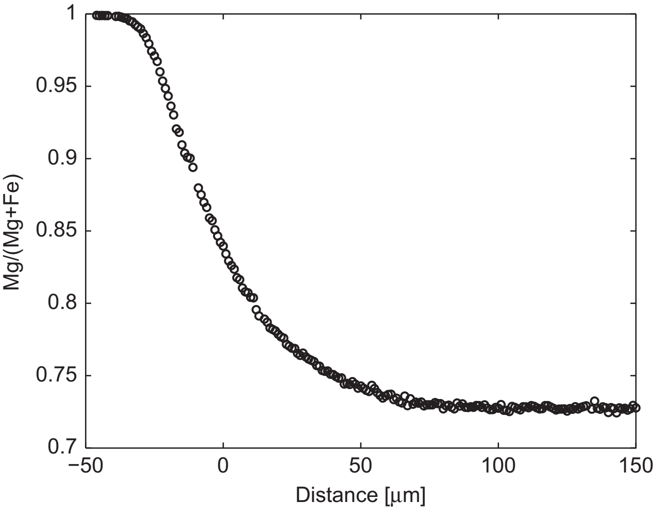

Fig. 5. Concentration profile of periclase–ferropericlase diffusion couples, annealed at 15 GPa, 1673 K for 27 h with a Mo sample capsule (K993), as a function of the position in the diffusion couple perpendicular to the original interface. The profile is asymmetric due to the strong compositional dependence of diffusivity.

equilibrates with respect to the local Mg/(Mg+Fe) composition under the externally-controlled oxygen fugacity. The obtained Fe^{3+} concentration along Mg–Fe interdiffusion profiles determined by the flank method is generally consistent with previous results on Fe^{3+} solubility by Bolfan-Casanova et al. (2006) and Otsuka et al. (2010), which further supports the conclusion that Fe^{3+} contents along diffusion profiles represent the Fe^{3+} solubility under the externally controlled oxygen fugacity conditions.

5.2. *Thermodynamic model*

In the previous paper (Otsuka et al., 2010), we presented a thermodynamic model of Fe^{3+} dissolution in ^{VI}[Mg, Fe^{2+}, Fe^{3+}, V]^{IV}[V, Fe^{3+}]$_2$[O] ferropericlase where Fe^{3+} occupies either octahedrally-coordinated cation sites or tetrahedrally-coordinated interstitial sites. The general charge neutrality condition is then written as

$$[\mathrm{Fe}^{\bullet}_{VI}]+6[\mathrm{Fe}^{\bullet\bullet\bullet}_{IV}]=2[V''_{VI}], \tag{2}$$

where $[\mathrm{Fe}^{\bullet}_{VI}]$, $[\mathrm{Fe}^{\bullet\bullet\bullet}_{IV}]$ and $[V''_{VI}]$ denote the concentration in atomic fraction of octahedral and tetrahedral Fe^{3+} and octahedral cation vacancies, respectively. Assuming Henry's law, the law of mass action of reactions for Fe^{3+} incorporation (Eqs. (5) and (6) in Otsuka et al., 2010) is given by

$$\mathrm{Fe}^{3+}=C[\mathrm{Fe}^{2+}]^l f^m_{O_2}\exp\left[-\frac{E^*+PV^*}{nRT}\right], \tag{3}$$

where E^* and V^* are the enthalpy of the reaction and volume change in the reaction for the solid part, respectively, and C, l, m, and n are constants. All of the values depend on the charge neutrality conditions (i.e., crystallographic sites of Fe^{3+}). The parameters l, m, and n are not independent but satisfy

$$l=4m=2/n, \tag{4}$$

following the constraint from the mass action equations. In the case where positively-charged defects are dominated by octahedral Fe^{3+} ($[\mathrm{Fe}^{\bullet}_{VI}]=2[V''_{VI}]$in Eq. (2)), those parameters are $l=2/3$, $m=1/6$, $n=3$, while in the case where they are dominated by tetrahedral Fe^{3+} ($3[\mathrm{Fe}^{\bullet\bullet\bullet}_{IV}]=[V''_{VI}]$ in Eq. (2)), $l=2/5$, $m=1/10$, $n=5$.

Considering the relatively large uncertainties in Fe^{3+} concentration of the obtained data, we approximated the thermodynamic model of Fe^{3+} concentration (Eq. (3)) using the single-valued parameters over the entire experimental range of conditions, without distinction between Fe^{3+} in octahedral and tetrahedral sites. We then assumed that the reaction enthalpy E^* depends linearly on Mg concentration:

$$E^*=X_{\mathrm{Mg}}E^*_{\mathrm{Mg}}+(1-X_{\mathrm{Mg}})E^*_{\mathrm{Fe}}, \tag{5}$$

where X_{Mg}=Mg/(Mg+Fe) and E^*_{Mg} and E^*_{Fe} are the reaction enthalpies for MgO and FeO, respectively. The compositional dependence in V^* was assumed to be negligible. We further assumed that $[Fe^{2+}]$ was set to be the Fe/(Mg+Fe) ratio, ignoring the contribution of Fe^{3+}, which then according to Eq. (3) gives

$$\mathrm{Fe}^{3+}=C\left(X_{\mathrm{Fe}}{}^4 f_{O_2}\right)^m\exp\left[\frac{-(1-X_{\mathrm{Fe}})\overline{E}^*_{\mathrm{Mg}}+X_{\mathrm{Fe}}\overline{E}^*_{\mathrm{Fe}}+P\overline{V}^*}{RT}\right], \tag{6}$$

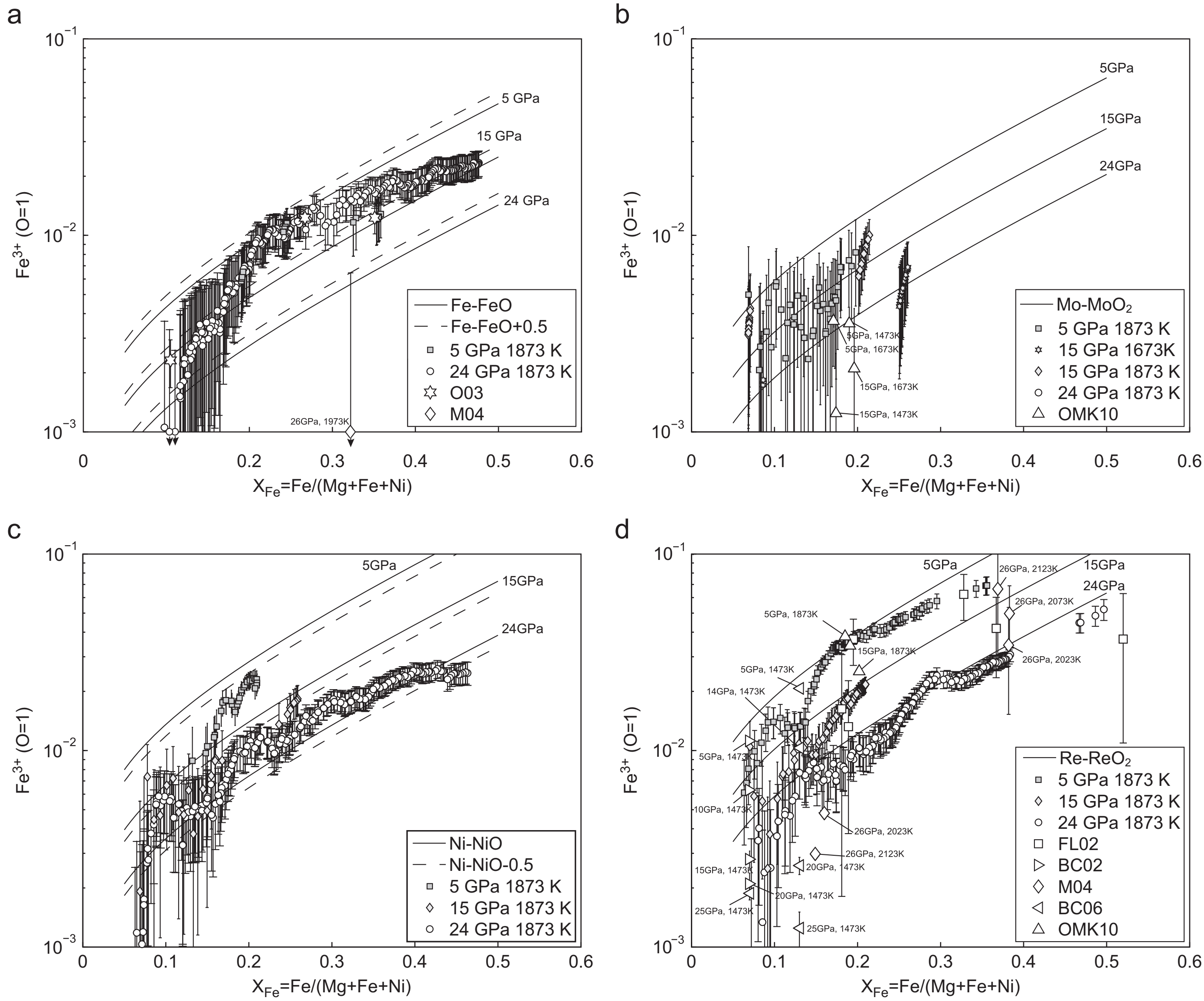

Fig. 6. Fe^{3+} concentrations along diffusion profiles in Fe capsules (a), Mo capsules (b), Ni capsules (c) and Re capsules (d) determined by the flank method plotted against Fe content compared with previously published values. Solid and dotted lines are calculated using Eq. (6) at 1873 K. Experimental conditions are 5–24 GPa, 1673–1873 K in Fe, Mo, Ni, Re capsules (this study), 5–25 GPa 1473 K in Re capsules (BC02: Bolfan-Casanova et al., 2002); 5–25 GPa, 1473–1873 K in Re capsules (BC06: Bolfan-Casanova et al., 2006); 25 GPa, 1973 K in Re capsules (FL02: Frost and Langenhorst, 2002), 26 GPa, 1973–2173 K in Re and Fe capsules (M04: McCammon et al., 2004a), room pressure, 1473 K in equilibrium with metallic Fe (O03:O'Neill et al., 2003); 5–15 GPa 1673–1873 K in Mo and Re capsules (OMK10: Otsuka et al., 2010). Solid arrows in (a) indicates that data below the plot range were moved to show the symbols.

where $\overline{E}^*_{Mg}$, $\overline{E}^*_{Fe}$ and $\overline{V}^*$ are the reaction enthalpy for MgO and FeO and volume change of the reaction divided by the parameter n, which satisfies $2m=1/n$ (Eq. (4)).

We determined oxygen fugacity of sample charges using solid-state redox equilibria between the metal capsule and corresponding oxide. Because of the uncertainty in thermodynamic data, the experiments with molten phases in the oxygen fugacity buffer were discarded from the regression of the Fe^{3+} equation. Based on the chemical composition described in the previous section, we considered the following chemical systems for the Re, Ni, Mo, and Fe capsules: Re–ReO_2, (Ni,Fe,Pt)–(Mg,Ni,Fe)O, (Mo,Fe,Pt)–(Mo,Fe,Pt)O_2, and (Fe,Pt)–(Mg,Fe)O, respectively. The thermodynamic database values of the end member components were taken from Robie et al. (1978). Activity coefficients were calculated using a regular solution model for (Mg,Fe,Ni)O and an asymmetric solution model for (Ni,Fe,Pt) and (Fe,Pt) alloys. Details regarding the calculation of oxygen fugacity are given in Supplementary Material, S5. Table 1 summarizes the obtained oxygen fugacity relative to the metal M and oxide MO_n buffer:

$$\Delta f_{O_2}[MMO]=\frac{2}{n}(\log a_{MO_n}-\log a_M), \tag{7}$$

where a is the activity of the relevant species. For each experiment with the Ni capsule, two oxygen fugacities were estimated separately using the redox equilibrium in Ni–NiO and Fe–FeO systems. The two obtained values of oxygen fugacity were averaged in the regression of Fe^{3+} concentration. Since no thermodynamic data were available for Mo_2O_3 to our knowledge, we treated Mo_2O_3 as MoO_2, which provides an upper bound for the actual oxygen fugacity. We confirmed that uncertainties in the results caused by the uncertainty in the Mo–Mo oxide buffer were small by carrying out the regression with and without the results from the Mo–Mo oxide buffer. This is partly because the number of measured Fe^{3+} values for the Mo–Mo oxide buffer is smaller than other buffers and partly because the oxygen fugacity for the Mo–MoO_2 buffer is not significantly different from that for Mo–Mo_2O_3 buffers near the phase boundary between Mo–Mo_2O_3 and Mo–MoO_2. MoO_2 is stable at least up to 5 GPa and 1873 K based on separate experiments that we conducted.

We fitted all of the experimental data with solid oxygen fugacity buffers to the model of equilibrium Fe^{3+} concentration (Eq. 6). In addition, in order to cover a wider range of conditions especially at low pressures, we fitted the following literature data combined with our experiments: Bolfan-Casanova et al. (2002, 2006), Dobson et al. (1998), Frost and Langenhorst (2002); McCammon (1994), McCammon et al. (2004b), O'Neill et al. (2003), Otsuka et al. (2010) and Speidel (1967). All of the literature data were selected based on the criterion that $Mg/(Mg+Fe) > 0.5$ and that the oxygen fugacity was within the stability field of ferropericlase. The results of the least squares fitting are summarized in Table 2. Note that in the case where the fit was made for data obtained in this study only, one of the reaction enthalpies, E_{Mg}, could not be determined because the experiments were conducted at the single temperature of 1873 K.

The fitting results are generally consistent with the thermodynamic model presented in our previous study (Otsuka et al., 2010). The parameter m, which is indicative of the charge neutrality conditions, was estimated to be 0.09 based on fitting of data obtained in this study and 0.11 for fitting of data including the previous studies. These values suggest that Fe^{3+} occupies tetrahedral sites more than octahedral sites under the experimental conditions. The obtained values of the normalized volume change of reaction $\overline{V}^{*}$ were 1.7 [cm^3/mol] based on fitting of data obtained in this study and 2.1 [cm^3/mol] based on fitting of data including the previous studies. These values are consistent with the thermodynamic model, predicting that the normalized volume change is the molar volume of (Mg,Fe)O (11.4 [cm^3/mol] for $(Mg_{0.8}Fe_{0.2})O$) times the normalization factor $2m=1/n$ (Eq. (4)).

Fig. 6 shows the fitting results using all of the literature data. The general trend of the data is consistent with the Fe^{3+} equation. Fe^{3+} concentration increases with increasing Fe content and oxygen fugacity for a given pressure and temperature. The dependence on pressure is clearly observed at the oxidized conditions imposed by Re and Ni capsules, while it is not as apparent at the reduced conditions imposed by Mo and Fe capsules. This is likely due to the relatively large uncertainties in the obtained Fe^{3+} concentrations at low Fe^{3+} concentration in the case of the Mo capsule. An interesting observation is that the Fe^{3+} concentration obtained in Fe capsules at 24 GPa and 1873 K (K1126) is significantly higher than the model prediction. It seems that the sample charge was significantly oxidized by the presence of molten Fe–Pt alloy. The oxygen fugacity estimated from the Fe^{3+} concentration using Eq. (6) is nearly 3.5 orders of magnitude higher than the Fe–(Mg,Fe)O buffer. In contrast, only a small effect on Fe^{3+} concentration is observed in the presence of molten oxide phases, such as (Mg,Fe,Ni)O at 5 GPa (K1027) and (Mg,Fe,Mo)-oxide at 5 and 24 GPa (K1028; K1124).

6. Implications for deep mantle diamond inclusions

We determined the equation of Fe^{3+} concentration as a function of temperature, pressure and Fe contents within a range of oxygen fugacity. We can use the established relationship to estimate the oxygen fugacity of ferropericlase inclusions preserved in natural diamonds from the lower mantle to infer the thermochemical state of diamond formation in the lower mantle. Inclusions of ferropericlase and pyroxene have been reported in a number of diamonds believed to have come from the lower mantle (Brenker et al., 2002; Frost and Langenhorst, 2002; Harte, 2010; Hayman et al., 2005; Hutchison et al., 2001; McCammon et al., 1997; McCammon et al., 2004b; Stachel et al., 2000; Walter et al., 2008, 2011). Since ferropericlase inclusions were encapsulated in diamond, it is reasonable to assume that Fe^{3+} concentration remained constant in a closed system during ascent of the diamonds.

Fig. 7 compares Fe^{3+} concentrations in ferropericlase inclusions measured by previous studies with the model estimates at pressures and temperatures near the top of the lower mantle (23 GPa and 1873–2073 K) with a range of oxygen fugacity. The adiabatic temperature of the top of the mantle is estimated to be 1960 ± 50 K (Katsura et al., 2010). Although the bulk lower mantle is thought to be at relatively reduced conditions due to the presence of (Fe,Ni) metal (e.g., Frost and McCammon, 2008), the majority of reported Fe^{3+} concentrations occur at oxidized conditions, as previously discussed in McCammon et al. (2004b). The redox conditions of ferropericlase were estimated assuming conditions of 23 GPa and 1873–2073 K to be 4.3–3.3 (± 1.2) log units and 3.2–

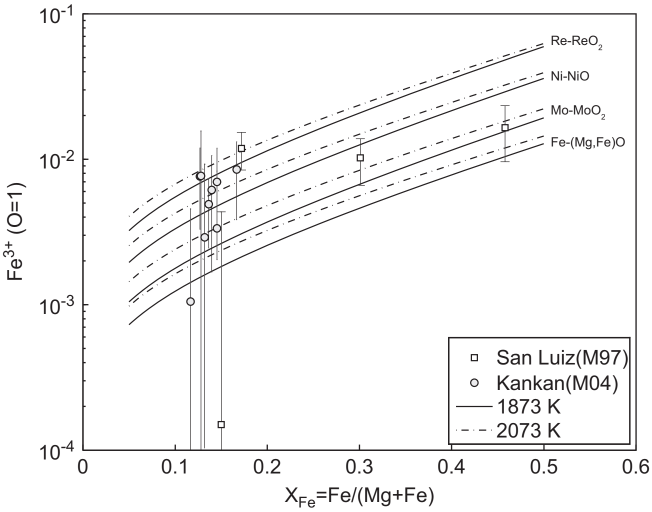

Fig. 7. Fe^{3+} concentration in ferropericlase inclusions from San Luiz (M97: McCammon et al., 1997) and Kankan (M04: McCammon et al., 2004b) compared with values calculated using Eq. (6) at a pressure of 23 GPa, temperature of 1873 and 2073 K, and oxygen fugacity buffered by Re–ReO_2, Ni–NiO, Mo–MoO_2, and Fe–(Mg,Fe)O.

Table 2
Fitting results for thermodynamic model of Fe^{3+} solubility.

C	m	E_{Mg} (kJ/mol)	E_{Fe} (kJ/mol)	V (cm^3/mol)	Data
$2.2(1)\times10^{-2}$	0.088(3)		−61(2)	1.67(3)	This study
$2.6(1)\times10^{-3}$	0.114(3)	−35(3)	−98(2)	2.09(3)	This study and previous studies*

() standard deviation of the last digit.

* Experimental data from this study, Bolfan-Casanova et al. (2002, 2006), Dobson et al. (1998), Frost and Langenhorst (2002) McCammon, (2004), McCammon et al. (2004a, O'Neill et al. (2003), Otsuka et al. (2010) and Speidel (1967).

2.6 (± 5.2) log units above the iron wüstite buffer (IW) for Kankan and San Luiz, respectively. The errors are 2σ standard deviations from the mean oxygen fugacity relative to IW weighted by errors propagated from Fe^{3+} concentration. Given the positive temperature dependence of Fe^{3+} concentration in ferropericlase in equilibrium with a metal-oxide buffer, deviation from the IW buffer decreases as temperature increases. Interestingly, such redox conditions coincide almost exactly with the upper stability limit of diamond in mantle peridotite at adiabatic or slightly superadiabatic temperature. As oxygen fugacity increases, diamond in peridotite is oxidized to carbonate (<1950 K) or carbonatite melt (>1950 K) according to the reaction:

$$3(Fe,Ni,Mg)O+C=MgCO_3+2(Fe,Ni)^0 \tag{8}$$

at approximately 3 log units above IW with negligible temperature and pressure dependence (Rohrbach and Schmidt, 2011). Consequently, the high Fe^{3+} concentrations preserved in ferropericlase inclusions suggest redox conditions where host diamonds precipitated from the oxidized state of CO_2 near the top of the lower mantle. We note that two of the ferropericlase inclusions reported in McCammon et al. (2004b) occur with $FeCO_3$ in the same diamond.

Diamond formation through decarbonation reactions in the lower mantle is consistent with the model of redox freezing and melting (Rohrbach and Schmidt, 2011), where redox conditions change dramatically due to the change in the capacity of mantle phases to incorporate Fe^{3+} (Frost and McCammon, 2008). They proposed that upwelling of carbon and oxygen-enriched domains in the vicinity of deeply-subducted oceanic lithosphere inevitably experiences carbonate-related redox melting near the top of the lower mantle, and that the resulting carbonatite melts are reduced to diamond when infiltrating the ambient mantle saturated with (Fe,Ni)-metal and carbide. We cannot, of course, exclude the possibility that the inclusions equilibrated at greater depths in the lower mantle. At such depths, however, the capacity of mantle phases to incorporate Fe^{3+} remains relatively high (Sinmyo et al., 2008a,b); hence the oxidation of diamond to produce carbonate melts may not occur in deeper parts of the lower mantle. In addition, a suite of mineral inclusions found in diamonds from the Juina kimberlite suggests that those diamonds crystallized in the upper part of the lower mantle (Walter et al., 2011).

Acknowledgment

This work was financially supported by the National Science Foundation under Grant no. EAR-0809330. We are grateful to Detlef Krauße and James Eckert for their assistance with electron microprobe analysis, to Hubert Schulze for sample preparation, and to George Amulele for multianvil experiments. We wish to thank Michael Walter and an anonymous reviewer for constructive reviews.

Appendix A. Supporting information

Supplementary data associated with this article can be found in the online version at http://dx.doi.org/10.1016/j.epsl.2012.11.030.

Reference

Andrault, D., Bolfan-Casanova, N., 2001. High-pressure phase transformations in the $MgFe_2O_4$ and Fe_2O_3–$MgSiO_3$ systems. Phys. Chem. Miner. 28 (3), 211–217.

Bolfan-Casanova, N., Mackwell, S., Keppler, H., McCammon, C., Rubie, D.C., 2002. Pressure dependence of H solubility in magnesiowüstite up to 25 GPa: implications for the storage of water in the Earth's lower mantle. Geophys. Res. Lett. 29 (10), 1449, http://dx.doi.org/10.1029/2001GL014457.

Bolfan-Casanova, N., McCammon, C.A., Mackwell, S., 2006. Water in transition zone and lower mantle minerals. In: Jacobsen, S.D., van der Lee, S. (Eds.), Earth's Deep Water Cycle. American Geophysical Union Geophysical Monograph Series, 168; pp. 57–68.

Bose, K., Ganguly, J., 1995. Quartz–Coesite transition revisited—reversed experimental-determination at 500–1200-degrees-C and retrieved thermochemical properties. Am. Mineral 80 (3–4), 231–238.

Brenker, F.E., Stachel, T., Harris, J.W., 2002. Exhumation of lower mantle inclusions in diamond: a TEM investigation of retrograde phase transitions, reactions and exsolution. Earth Planet. Sci. Lett. 198, 1–9.

Cottrell, E., Kelley, K.A., Lanzirotti, A., Fischer, R.A., 2009. High-precision determination of iron oxidation state in silicate glasses using XANES. Chem. Geol. 268, 167–179, http://dx.doi.org/10.1016/j.chemgeo.2009.08.008.

de Koker, N., Stixrude, L., 2010. Theoretical computation of diffusion in minerals and melts. Rev. Mineral. Geochem. 72 (1), 971–996 910.2138/rmg.2010.2172.2122.

Dobson, D.P., Cohen, N.S., Pankhurst, Q.A., Brodholt, J.P., 1998. A convenient method for measuring ferric iron in magnesiowüstite (MgO–$Fe_{1-x}O$). Am. Mineral. 83 (7-8), 794–798.

Dobson., D.P., Richmond, N.C., Brodholt, J.P., 1997. A high-temperature electrical conduction mechanism in the lower mantle phase $(Mg,Fe)O_{1-x}$. Science 275 (5307), 1779–1781.

Enders, M., Speer, D., Maresch, W.V., McCammon, C.A., 2000. Ferric/ferrous iron ratios in sodic amphiboles: Mössbauer analysis, stoichiometry-based model calculations and the high-resolution microanalytical flank method. Contrib. Mineral. Petrol. 140 (2), 135–147, http://dx.doi.org/10.1007/s004100000179.

Fei, Y., Van Orman, J., Li, J., van Westrenen, W., Sanloup, C., Minarik, W., Hirose, K., Komabayashi, T., Walter, M., Funakoshi, K., 2004. Experimentally determined postspinel transformation boundary in Mg_2SiO_4 using MgO as an internal pressure standard and its geophysical implications. J. Geophys. Res. 109 (B02305), http://dx.doi.org/10.1029/2003JB002562.

Frost, D.J., Langenhorst, F., 2002. The effect of Al2O3 on Fe-Mg partitioning between magnesiowüstite and magnesium silicate perovskite. Earth Planet. Sci. Lett 199, 227–241.

Frost, D.J., McCammon, C.A., 2008. The redox state of Earth's mantle. Annu. Rev. Earth Planet. Sci. 36, 389–420, http://dx.doi.org/10.1146/annurev.earth.36.031207.124322.

Gessmann, C.K., Rubie, D.C., McCammon, C.A., 1999. Oxygen fugacity dependence of Ni, Co, Mn, Cr, V, and Si partitioning between liquid metal and magnesiowüstite at 9–18 GPa and 2200 degrees C. Geochim. Cosmochim. Acta 63 (11–12), 1853–1863.

Gordon, R.S., 1973. Mass-transport in diffusional creep of ionic solids. J. Am. Ceram. Soc. 56 (3), 147–152.

Hansen, K.W., Cutler, I.B., 1966. Electrical conductivity in $Fe_{1-x}O$–MgO solid solutions. J. Am. Ceram. Soc. 49 (2), 100–102.

Harte, B., 2010. Diamond formation in the deep mantle: the record of mineral inclusions and their distribution in relation to mantle dehydration zones. Mineral. Mag. 74 (2), 189–215, http://dx.doi.org/10.1180/minmag.2010.074.2.189.

Hayman, P.C., Kopylova, M.G., Kaminsky, F.V., 2005. Lower mantle diamonds from Rio Soriso (Juina area, Mato Grosso, Brazil). Contrib. Mineral. Petrol. 149, 430–445, http://dx.doi.org/10.1007/s00410-005-0657-8.

Hazen, R.M., Jeanloz, R., 1984. Wustite ($Fe_{1-x}O$): a review of its defect structure and physical properties. Rev. Geophys. 22 (1), 37–46.

Hilbrandt, N., Martin, M., 1998. High temperature point defect equilibria in iron-doped MgO: an in situ Fe–K XAFS study on the valance and site distribution of Iron in $(Mg_{1-x}Fe_x)O$. Ber. Bunsen. Gese. Phys. Chem. 102, 1747–1759.

Höfer, H.E., Brey, G.P., 2007. The iron oxidation state of garnet by electron microprobe: its determination with the flank method combined with major-element analysis. Am. Mineral. 92 (5–6), 873–885, http://dx.doi.org/10.2138/am.2007.2390.

Höfer, H.E., Brey, G.P., Schulzdobrick, B., Oberhansli, R., 1994. The determination of the oxidation-state of iron by the electron-microprobe. Eur. J. Mineral. 6 (3), 407–418.

Höfer, H.E., Weinbruch, S., McCammon, C.A., Brey, G.P., 2000. Comparison of two electron probe microanalysis techniques to determine ferric iron in synthetic wüstite samples. Eur. J. Mineral. 12 (1), 63–71.

Hutchison, M.T., Hursthouse, M.B., Light, M.E., 2001. Mineral inclusions in diamonds: associations and chemical distinctions around the 670-km discontinuity. Contrib. Mineral. Petrol. 142, 119–126, http://dx.doi.org/10.1007/s004100100279.

Inoue, T., Irifune, T., Higo, Y., Sanehira, T., Sueda, Y., Yamada, A., Shinmei, T., Yamazaki, D., Ando, J., Funakoshi, K., Utsumi, W., 2006. The phase boundary between wadsleyite and ringwoodite in Mg_2SiO_4 determined by in situ X-ray diffraction. Phys. Chem. Mineral. 33 (2), 106–114, http://dx.doi.org/10.1007/s00269-005-0053-y.

Irifune, T., Shinmei, T., McCammon, C.A., Miyajima, N., Rubie, D.C., Frost, D.J., 2010. Iron partitioning and density changes of pyrolite in Earth's lower mantle. Science 327 (5962), 193–195, http://dx.doi.org/10.1126/science.1181443.

Katsura, T., Kimura, S., 1965. Equilibria in system FeO–Fe_2O_3–MgO at 1160 Degrees C. Bull. Chem. Soc. Jpn. 38 (10), 1664–1670.

Katsura, T., Yoneda, A., Yamazaki, D., Yoshino, T., Ito, E., 2010. Adiabatic temperature profile in the mantle. Phys. Earth. Planet. Inter. 183, 212–218, http://dx.doi.org/10.1016/j.pepi.2010.07.001.

Katsura, T., Yamada, H., Nishikawa, O., Song, M.S., Kubo, A., Shinmei, T., Yokoshi, S., Aizawa, Y., Yoshino, T., Walter, M.J., Ito, E., Funakoshi, K., 2011. Olivine-wadsleyite transition in the system $(Mg,Fe)_2SiO_4$. J. Geophys. Res. 162 (6), 1249–1257, http://dx.doi.org/10.1007/s00410-011-0649-9.

Leinenweber, K., Mosenfelder, J., Diedrich, T., Soignard, E., Sharp, T.G., Tyburczy, J.A., Wang, Y., 2006. High-pressure cells for in situ multi-anvil experiments. High Pressure Res 26 (3), 283–292, http://dx.doi.org/10.1080/08957950600894671.

Longo, M., McCammon, C.A., Jacobsen, S.D., 2011. Iron Oxidation State in (Mg,Fe)O using the Flank Method: I. Calibration. Contrib. Mineral. Petrol. 162 (6), 1249–1257, http://dx.doi.org/10.1007/s00410-011-0649-9.

Mackwell, S., Bystricky, M., Sproni, C., 2005. Fe–Mg interdiffusion in (Mg,Fe)O. Phys. Chem. Mineral. 32 (5–6), 418–425, http://dx.doi.org/10.1007/s00269-005-0013-6.

McCammon, C.A., 1994. Mössbauer spectroscopy of quenched high-pressure phases: Investigating the Earths interior. Hyper. Inter. 90 (1-4), 89–105.

McCammon, C., Hutchison, M., Harris, J., 1997. Ferric iron content of mineral inclusions in diamonds from Sao Luiz: a view into the lower mantle. Science 278 (5337), 434–436.

McCammon, C.A., 2004. Mössbauer spectroscopy: applications. In: Beran, A, Libowitsky, E (Eds.), Spectroscopic Methods in Mineralogy, EMU Notes in Mineralogy, vol. 6; pp. 369–398.

McCammon, C.A., Lauterbach, S., Seifert, F., Langenhorst, F., van Aken, P.A., 2004a. Iron oxidation state in lower mantle mineral assemblages—I. Empirical relations derived from high-pressure experiments. Earth Planet. Sci. Lett. 222 (2), 435–449, http://dx.doi.org/10.1016/j.epsl.2004.03.018.

McCammon, C.A., Stachel, T., Harris, J.W., 2004b. Iron oxidation state in lower mantle mineral assemblages—II. Inclusions in diamonds from Kankan, Guinea. Earth Planet. Sci. Lett. 222 (2), 423–434, http://dx.doi.org/10.1016/j.epsl.2004.03.019.

O'Neill, H.S., Pownceby, M.I., McCammon, C.A., 2003. The magnesiowüstite: iron equilibrium and its implications for the activity-composition relations of $(Mg,Fe)_2SiO_4$ olivine solid solutions. Contrib. Mineral Petrol. 146 (3), 308–325, http://dx.doi.org/10.1007/s00410-003-0496-4.

Otsuka, K., McCammon, C.A., Karato, S., 2010. Tetrahedral occupancy of ferric iron in (Mg,Fe)O: implications for point defects in the Earth's lower mantle. Phys. Earth Planet. Inter 180 (3–4), 179–188, http://dx.doi.org/10.1016/j.pepi.2009.10.005.

Rubie, D.C., Karato, S., Yan, H., O'Neill, H.S.C., 1993. Low differential stress and controlled chemical environment in multianvil high-pressure experiments. Phys. Chem. Mineral. 20 (5), 315–322.

Robie, R.A., Hemingway, B.S., Fisher, J.R., 1978. Thermodynamic properties of minerals and related substances at 298.15 K and 1 bar (105 Pa) pressure and at higher temperatures. US Government Printing Office, US Geological Survey Bulletin, 1452, Washington, 456 pp.

Rohrbach, A., Schmidt, M.W., 2011. Redox freezing and melting in the Earth's deep mantle resulting from carbon–iron redox coupling. Nature 472, 209–212, http://dx.doi.org/10.1038/nature09899.

Sinmyo, R., Hirose, K., Nishio-Hamane, D., Seto, Y., Fujino, K., Sata, N., Ohishi, Y., 2008a. Partitioning of iron between perovskite/postperovskite and ferropericlase in the lower mantle. J. Geophys. Res. 113 (B11), http://dx.doi.org/10.1029/2008JB005730.

Sinmyo, R., Ozawa, H., Hirose, K., Yasuhara, A., Endo, N., Sata, N., Ohishi, Y., 2008b. Ferric iron content in $(Mg,Fe)SiO_3$ perovskite and post-perovskite at deep lower mantle conditions. Am. Mineral. 93 (11–12), 1899–1902.

Speidel, D.H., 1967. Phase equilibria in system MgO–FeO–Fe_2O_3: the 1300 degrees C isothermal section and extrapolations to other temperatures. J. Am. Ceram. Soc 50 (5), 243–248.

Srečec, I., Ender, A., Woermann, E., Gans, W., Jacobsson, E., Eriksson, G., Rosen, E., 1987. Activity-composition relations of the Magnesiowüstite solid–solution series in equilibrium with metallic iron in the temperature-range 1050–1400-K. Phys. Chem. Mineral. 14 (6), 492–498.

Stachel, T., Harris, J.W., Brey, G.P., Joswig, W., 2000. Kankan diamonds (Guinea) II: lower mantle inclusion parageneses. Contrib. Mineral. Petrol. 140 (1), 16–27.

Tremper, R.T., Giddings, R.A., Hodge, J.D., Gordon, R.S., 1974. Creep of polycrystalline MgO–FeO–Fe_2O_3 solid–solutions. J. Am. Ceram. Soc. 57 (10), 421–428.

van Aken, P.A., Liebscher, B., 2002. Quantification of ferrous/ferric ratios in minerals: new evaluation schemes of Fe L_{23} electron energy-loss near-edge spectra. Phys. Chem. Mineral.29, 188–200, http://dx.doi.org/10.1007/s00269-001-0222-6.

Van Orman, J.A., Li, C., Crispin, K.L., 2009. Aluminum diffusion and Al-vacancy association in periclase. Phys. Earth Planet. Inter. 172 (1–2), 34–42, http://dx.doi.org/10.1016/j.pepi.2008.03.008.

Walter, M.J., Kohn, S.C., Araujo, D., Bulanova, G.P., Smith, C.B., Gaillou, E., Wang, J., Steele, A., Shirey, S.B., 2011. Deep mantle cycling of oceanic crust: evidence from diamonds and their mineral inclusions. Science 334 (6052), 54–57, http://dx.doi.org/10.1126/science.1209300.

Walter, M.J.., Bulanova, G.P., Armstrong, L.S., Keshav, S., Blundy, J.D., Gudfinnsson, G., Lord, O.T., Lennie, A.R., Clark, S.M., Smith, C.B., Gobbo, L., 2008. Primary carbonatite melt from deeply subducted oceanic crust. Nature 454 (31), 622–626, http://dx.doi.org/10.1038/nature07132.

Wiser, N.M., Wood, B.J., 1991. Experimental-determination of activities in Fe–Mg olivine at 1400-K. Contrib. Mineral. Petrol. 108 (1–2), 146–153.

Wood, B.J., 2000. Phase transformations and partitioning relations in peridotite under lower mantle conditions. Earth Planet. Sci. Lett 174 (3–4), 341–354.

Wood, B.J., Nell, J., 1991. High-temperature electrical-conductivity of the lower-mantle phase (Mg,Fe)O. Nature 351 (6324), 309–311.

Zhang, J., Li, B., Utsumi, W., Liebermann, R.C., 1996. In situ X-ray observations of the coesite stishovite transition: reversed phase boundary and kinetics. Phys. Chem. Mineral. 23 (1), 1–10.